Thermal Charging Rate of Composite Wax-Expanded Graphite Phase Change Materials

Jason HIRSCHEY[1], Navin KUMAR[2], Tim LACLAIR[2], Kyle R. GLUESENKAMP[2]*, Samuel GRAHAM[1]

[1]Georgia Institute of Technology,
Atlanta, GA, USA
Jhirschey13@gatech.edu

[2]Oak Ridge National Laboratory,
Oak Ridge, TN, USA
gluesenkampk@ornl.gov

* Corresponding Author

ABSTRACT

Phase change materials (PCMs) are valuable for their ability to store heat nearly isothermally around their phase transition temperature. PCMs are at the core of latent heat thermal energy storage (LHTES) systems, which provide the ability to buffer high thermal loads or decouple the time when heating or cooling is needed from when it is produced. Thermal charging and discharging of LHTES systems often employ a constant temperature source, and the rate at which heat can be exchanged is dependent on the thermophysical properties of the PCM. For graphite composite PCMs, the high thermal conductivity of the graphite enables an increased heat transfer rate through the material, but its presence displaces PCM which reduces the effective volumetric latent heat of the composite relative to the pure PCM. This results in a tradeoff between thermal power and volumetric energy storage capacity. The thermal charging rate is the average thermal energy stored in the material for some elapsed time. In this study, composite PCMs of compressed expanded natural graphite (CENG) and n-Octadecane are studied. Samples with varying CENG mass fractions were synthesized and the thermal charging rate was measured under a constant temperature boundary condition. For evaluation of the expanded graphite-PCM composite, one boundary of the material was exposed to a 50°C constant temperature plate, above the 27.5°C melting temperature of the PCM. The melting front progression [mm-s^{-1}] and the thermal charging rate [W-cm^{-2}] of the PCM were determined, and the results were compared with analytical predictions for the 1-D semi-infinite phase change. For CENG addition up to 5.75% mass fraction, a 450% thermal conductivity increase was observed with a only 5% decrease in volumetric energy density as compared to pure octadecane. The average thermal charging rate was increased by over 430% for the melt to penetrate a depth of 22 mm. The experimental results matched analytical predictions, indicating that higher CENG fractions can be evaluated using analytical approaches.

1. INTRODUCTION

Low temperature (<100°C) latent heat thermal energy storage (LHTES) can be useful for space heating and space cooling applications by decoupling the operation of an HVAC system to the use of its output. At their core, LHTES typically use phase change materials (PCMs) which can store significant amounts of near-isothermal heat in the latent heat of phase change. Many PCMs that undergo a phase change in this temperature range suffer from low thermal conductivity, particularly in the liquid state. This hinders the rate at which thermal energy can be exchanged in the LHTES and limits their operating capacity.

Much work has been done to increase the thermal charging rate of PCMs in LHTES systems, namely in heat exchangers of various configurations. Researchers have utilized intricate extended surfaces and finned structures which often add complexity to the system and may increase overall LHTES cost. Mahdi et al. (2018) investigated several fin configurations of horizontal triplex-tube heat exchangers, and modeled the liquid fraction and temperature

distribution under constant temperature boundaries at the inner and outer surfaces. Abdulateef et al. (2019) optimized the geometrical fin structure of a triplex-tube heat exchanger with a paraffin PCM infused with alumina nanoparticles as a means of reducing the fin material.

Other researchers are developing PCM composites to enhance the thermal conductivity over that of pure PCM. This can include metallic foams. Esapour et al. (2018) modeled a quasi-shell and tube heat exchanger with metallic foam impregnated with PCM in the shell portion of the heat exchanger. The researchers modeled the time to fully melt the PCM under various metallic foam porosity and identified tube geometries that lead to faster thermal charging.

Liang et al. (2018) developed a superhydrophobic copper foam to enhance the thermal conductivity of organic PCMs by nearly 10 times, but also serve as a shape-stable supporting network that prevents PCM leakage thereby reducing the need for exterior packaging. Rao et al. (2018) employed copper particles and foam on paraffin PCM microencapsulated in a polyurethane shell.

Mallow et al. (2018) performed thermal charging measurements on paraffin wax PCM enhanced with both metallic foams and CENG. They utilized a constant power source to charge the PCM and measured the temperature rise with time near the heater and at the far end of the sample. They showed that samples with higher thermal conductivity took less time to melt fully.

Zeng et al. (2018) increased the thermal conductivity of an organic PCM eutectic composed of *m*-Erythritol and D-mannitol by 408% with exfoliated graphite. Wang et al. (2018) increased the thermal conductivity of polyethylene glycol with metal-organic frameworks nanoparticles on copper nanotubes. Fashandi and Leung (2018) utilized a combination of graphene nanoplatelets and hexagonal boron nitride to increase the thermal conductivity of the inorganic salt hydrate sodium acetate trihydrate.

Most papers investigating the thermal charging capability of PCMs, including those above, look at the time to fully melt the PCM in a fixed geometry or track the liquid fraction during the melting process. Yang et al. (2018) examined metallic foam-enhanced ice storage. They showed the melting and freezing time of the PCM was significantly reduced with the metallic foam and tracked the melt-/freeze-front visually, extrapolating this to determine the melted fraction during the phase transition. These researchers tracked the boundary wall heat flux, referred to as the thermal charging rate in this current paper, and showed the metallic foam with the lowest pore density and highest thermal conductivity resulted in the highest thermal charging rate. The planar geometry used by the authors is most similar to what is attempted and presented by this current paper.

With the introduction of these additives to influence the thermal conductivity, some PCM is displaced. This will have implications for the latent heat, specific heat, and density of the resulting composite. For a LHTES, all these thermophysical properties play a role in the rate at which thermal energy can be exchanged in the system and the total energy that can be stored per unit volume.

The objective of this paper is to experimentally compare the thermal charging rate of a composite PCM to the analytical 1-D semi-infinite phase change solution and show that small quantities of CENG can drastically improve the PCM composite thermal charging performance without significantly sacrificing thermal storage capacity. The thermal charging is the average thermal power pulled into the system for the elapsed time the PCM is exposed to the constant temperature boundary. The composite PCMs used in this sample are composed of compressed expanded natural graphite and n-octadecane, an organic wax PCM.

2. EXPERIMETAL SETUP

2.1 Test Setup

The test setup shown in **Figure 1** is designed to expose a PCM composite to a bounding surface of uniform temperature above the PCM melting temperature. The temperature of the PCM composite is measured at various distances from the bounding surface. This enables calculation of the rate at which heat enters the composite (the thermal charging rate) and tracking of the melt-front, solid-liquid interface. The constant temperature heating surface is made of aluminum with a steady flow of water at constant temperature through internal channels. The water source is an 8-

gallon, heater-only PID temperature-controlled bath with stability of ±0.2°C. The large thermal mass of this water together with minimal losses leads to slow PID response time which may account for some temperature drift in this aluminum block temperature.

The PCM material is contained in a thin-walled polypropylene cylinder of 35 mm diameter and with a polypropylene cap. The cylinder was placed in an insulated sleeve for testing with its bottom face left exposed. Aluminum foil was epoxied to the bottom of the cylinder to seal the container, contain the PCM, and make for good contact with the constant temperature plate.

Expanded graphite was compressed into the cylinder to specific volume fractions. The PCM then infiltrated into the graphite by means of a vacuum oven, a process which has shown to be successful at creating similar graphite-wax PCMs with minimal void fraction (Mallow *et al.*, 2018). Once this process is complete and the PCM has solidified completely, three 1/32" holes were drilled into the polypropylene walls and composite PCM for thermocouple placement. The thermocouples reached the centerline of the cylinder and were placed closer to the heated surface (far from the opposite surface) to minimize edge effects caused by a bounded, not semi-infinite, system.

A thin layer of silicone heat transfer grease was spread on the bottom surface of the aluminum foil to reduce thermal contact resistance between the plate and the PCM. In addition, a 200 g mass was placed atop the PCM sample to apply uniform pressure across all samples where the PCM sample contacts the plate.

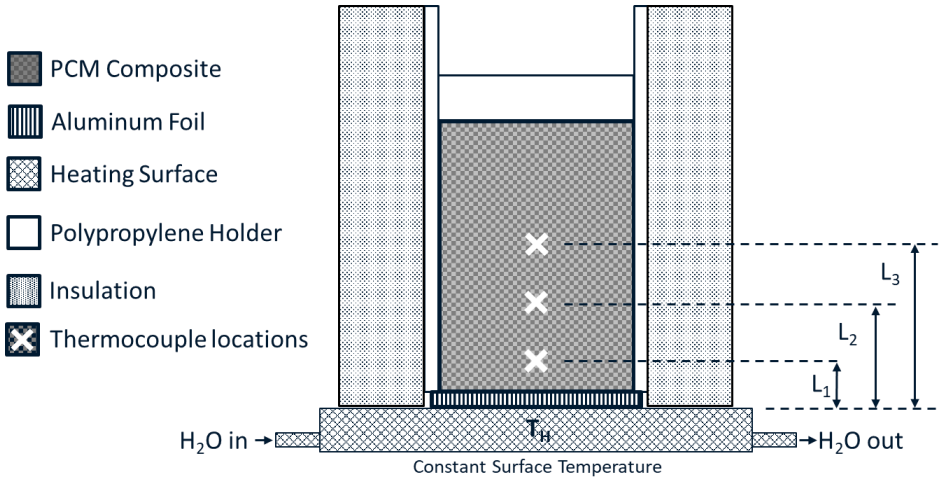

Figure 1: Thermal charging experimental setup

The three thermocouple placement holes are measured from the bottom heating surface as shown in Figure 1. Care was made to make the thermocouple spacing similar across samples, but some deviation in the exact location exists. Table 1 shows the thermocouple locations for the samples measured after their placement.

Table 1: Thermocouple locations

Sample ID	Thermocouple 1, L_1 (mm)	Thermocouple 2, L_2 (mm)	Thermocouple 3, L_3 (mm)
A	8.6	16.4	22.3
B	8.7	16.3	23.6
C	8.6	16.4	21.8

During each test, water was run through the block for at least 30 minutes to ensure the block and all piping reaches a steady state temperature. The sample itself is kept in an isolated chamber and the three thermocouples monitored to ensure the sample is at a uniform temperature. Data recording is started, allowed to run for several minutes, and the sample quickly transferred from its chamber to the constant temperature block. If there is a delay in this process, the

sample is misaligned on the plate, or extraneous circumstances cause some disruption, the test is aborted and restarted.

The sample sits on the plate for the duration of the test. It is monitored to ensure it does not shift, change position, or leak during the phase change process. The test runs until all three thermocouples register a completed phase change, plus approximately 30 minutes. Data collection is stopped. Once completed, the sample is removed from the block and allowed to cool and freeze at room temperature.

2.2 Materials

The cylindrical polypropylene holder is a 140 mL laboratory syringe with the plunger removed and the fluid-dispensing tip and adjoining cap severed to create a hollow cylinder. These syringes are thin-walled, low thermal conductivity, inert, and the demarcations useful for loading the graphite and PCM uniformly. The thin walls and low thermal conductivity are important for reducing the thermal mass at the edges of the sample and prevent a thermal finning effect, both of which can skew the results. The plunger is useful for packing the graphite by perfectly matching the inner diameter. The CENG worms are sourced as-is from the manufacturer; no chemical pretreatment or modifications were made. Prior to creating the sample, the CENG was heated in an oven to remove any moisture that may be present. 99.9% pure n-Octadecane was procured from a laboratory chemical supplier. The entire contents of the 2 kg bottle were fully melted and stirred to ensure the octadecane used across all tests was uniform.

Type T thermocouples were used for all measurements. The thermocouples in the samples are 1/32” in diameter to minimize their presence in the samples. The plate was measured using a bead-welded 24 AWG type T thermocouple with silicone thermal grease ensuring good thermal contact. This plate thermocouple was affixed to the same position across all tests and samples. The samples were wrapped in ¾” foam insulation to minimize heat loss during the experiments. The aluminum foil and thermocouples were epoxied with high strength inert epoxy. Data was acquired at a rate of 1.2 Hz.

2.3 Sample Preparation

The preparation of all PCM composites followed the same process and are identical in form factor and packaging. The packaging is designed to be PCM leak tight. The syringes were prepped by removing the nozzles and roughing the bottom inch of the outside with 400 grit sandpaper which allows the epoxy to adhere and provide a leak-proof seal with the aluminum foil. Likewise, the aluminum foil was lightly sanded with 800 grit sandpaper to allow the epoxy to better adhere. The aluminum foil and cylinders were then epoxied together with extreme care to prevent epoxy on the foil faces in contact with the sample and the plate and inside the cylinder; the epoxy formed a bead around the base of the cylinder. A known mass of CENG was compressed into the open end of the cylinder with the plunger of the syringe to a final bulk CENG volume of 100 mL as read from the demarcations on the syringe. The CENG-filled cylinders were weighed, and this value recorded. The samples were then infiltrated with octadecane (melting point, 27.5°C) standing upright in a low temperature vacuum oven at 50°C. To prevent the graphite from floating upwards away from the aluminum foil, the plunger was taped in place to hold the graphite bulk volume at 100 mL. A small 1/16” hole was drilled in the plunger to allow the octadecane to flow into the graphite. The samples were left in the oven for 4 hours, or until the liquid level of octadecane stopped falling. Once taken out of the oven, the remaining liquid octadecane was skimmed off the top of the CENG and the sample allowed to cool and solidify completely. Lastly, the composite samples were weighed; the difference between the final mass and that of the CENG was used to determine the mass of octadecane. The compositions of the three samples are shown in Table 2.

Table 2: Composition of PCM samples

Sample ID	CENG Mass (g)	CENG Mass Fraction (g/g)	CENG Bulk Density ($kg\text{-}m^{-3}$)	Octadecane Mass (g)
A	4.848	5.75%	48.5	79.5
B	1.967	2.38%	19.7	80.6
C	1.054	1.29%	10.5	80.9

By comparing the expected value of octadecane to the measured value, the void space of these samples is less than 1%, indicating the graphite is fully saturated with octadecane. Next, the three 1/32” holes were drilled into the walls

of the cylinder and into the PCM composite for the thermocouple placement. Care was taken to ensure the holes were perpendicular to the cylinder walls and did not deviate in the axial direction in the sample. The thermocouples were inserted into the holes and more epoxy applied around the thermocouple holes to seal them and lock the thermocouples in place. The last step is to place the samples upright into a low temperature oven at 50°C to leak test the sample. If any octadecane escapes between the cylinder and the aluminum or through the thermocouple holes, the sample is considered failed and scrapped. This step also melts the PCM around the thermocouples to provide good thermal contact, ensuring accurate measurements during the test.

Effective thermophysical properties of the PCM composite are used in the heat transfer model and are calculated from the mass and volume fractions of the constituents. The effective specific heat and latent heat are a function of the mass fractions, m_γ, of the CENG and octadecane as shown by equations (1) and (2). The thermophysical values for octadecane are taken from literature from (Faden et al., 2019), and for graphite from (Incropera & DeWitt, 2002).

$$c_p = m_{\gamma,CENG} * c_{p,CENG} + m_{\gamma,octadecane} * c_{p,octadecane} \quad (1)$$

$$H_f = m_{\gamma,octadecane} * H_{f,octadecane} \quad (2)$$

The density of the PCM in the sample is assumed constant at the bulk sample density of the composite in the melted state. Lastly, the thermal conductivity is estimated through interpolation of data of CENG-wax composites created in the same vacuum oven infiltration process from (Mallow et al., 2018). Since changes in the octadecane thermal conductivity with phase are small compared to the bulk conductivity, the thermal conductivity of the graphite component is assumed to dominate, and the effective conductivity is assumed to be constant. The thermal conductivity values calculated agree with similar samples measured using the ASTM D5470 standard (not reported here).

The thermophysical properties of the samples are shown in Table 3. Note that with the small addition of CENG in these samples, the specific heat and volumetric storage capacity change by about 5% relative to the pure PCM, while the thermal conductivity increases by a factor of about 4, which provides an indication of the favorable tradeoff of the CENG enhancement on the heat for energy storage vs. power capabilities.

Table 3: Composite PCM thermophysical properties

Sample ID	Calculated Specific Heat (J/g-K)		Calculated Latent Heat (J/g)	Interpolated Thermal Conductivity (W/m-K)	Measured Density (kg/m^3)	Calculated Volumetric Latent Heat Storage Capacity (J/cm^3)
	Liquid	Solid				
A	2.1	1.7	230	0.91	845	194.4
B	2.2	1.8	238	0.44	826	196.6
C	2.2	1.8	241	0.31	820	197.6

3. ANALYTICAL MODEL

This work is designed to experimentally test the 1-D semi-infinite planar phase change problem for PCM composites of varying composition, commonly known as the Stefan problem. This analytical solution is easily solvable and has been derived extensively (Hahn & Özişik, 2012). The boundary condition to this problem is a constant temperature imposed at one surface of a semi- infinite volume of PCM. The initial condition is that at all points, the PCM is at a uniform temperature at the initial time.

$$T_l(x = 0, t > 0) = T_o \quad (3)$$
$$T_s(x \to \infty, t > 0) = T_i \quad (4)$$
$$T_l(x = 0, t = 0) = T_i \quad (5)$$

At the melting interface, two conditions must be met: 1) the solid and liquid temperature are equal to the melting temperature, and 2) the rate of heat into and out of the interface must equal to the progression of the interface accounting for the latent heat. These conditions are shown here.

$$T_l(x = s(t), t > 0) = T_s(x = s(t), t > 0) = T_m \quad (6)$$

$$-k_s \frac{dT_s}{dx}\Big|_{s(t)} + k_l \frac{dT_l}{dx}\Big|_{s(t)} = \rho_l H_f \frac{ds}{dt} \quad (7)$$

There are many differences between this analytical model and the experimental setup and are listed below:

- The experimental setup is not semi-infinite in length. This is expected to introduce some edge effects. To help compensate for this shortcoming, the PCM samples are intentionally oversized at nearly 10 cm of material, but the measurements only occur in the bottom 2.5 cm near the heated surface.
- Similarly, the PCM is not infinite in the planar direction. Again, this is expected to introduce some edge effects. The thin-walled polypropylene cylinder was chosen to minimize this heat loss (as compared to a more readily accessible metallic pipe), and a thick layer of insulation blanketed the entire system. The thermocouples were inserted into the centerline of the cylinder to reduce the edge effects near the walls.
- The initial temperature is not perfectly uniform throughout the samples. The insulted samples were placed sideways in an insulated box for several hours prior to the test. This helped minimize any temperature gradients due to the sample bottom surface contacting any other surface and reduced the fluctuations in sample initial temperature with room ambient temperature.
- The bounding surface is not a perfectly constant temperature. The constant temperature block is heated by running water through interior channels. The water source is an 8-gallon, heater-only PID temperature-controlled bath. The large thermal mass of this water coupled with minimal losses leads stable temperature.
- Along the same vein, there is not perfect thermal contact between the PCM composite and this aluminum block. Additionally, there is the aluminum foil between the two which is not accounted for by the analytical model. The aluminum foil is necessary to prevent the octadecane from spilling out of the holder when melted. Silicone thermal grease is employed to reduce the contact resistance between the plate and the foil. Care was taken when creating the samples to ensure a flat bottom PCM surface. A 200 g weight applies even pressure between the sample and plate. And the thermal resistance of the aluminum is negligible relative to the PCM composite.
- The PCM in the model has one discrete melting temperature. n-Octadecane completes the melting process across a range of temperatures, commonly called a temperature glide. The model does not account for this. Octadecane has extensive documentation on its temperature glide (Faden et al., 2019). In the model used to compare the experimental results to the analytical solution, the melting temperature is chosen to be the temperature at which the samples complete the melting process, often indicated by an inflection point on a temperature vs. time plot. This is approximately 27.5°C for this sample set.

Despite the limitations in matching the experimental testing conditions to the analytical solution assumptions, the comparison between the two is useful to validate that the analytical solution as a good method for determining relative PCM composite performance. By following the derivation of the analytical solution, the melting interface is shown to be a function of the liquid thermal diffusivity, time, and a parameter, λ, which is solved numerically and by applying the interface boundary conditions (Hahn & Özişik, 2012). Equation (8) shows the melt-front interface as a function of time, *s(t)*.

$$s(t) = \lambda\sqrt{4\alpha_l t} \quad (8)$$

To determine the thermal total energy stored in the PCM, the latent and sensible heat are calculated by equations (9) through (11). Equation (9) shows that the latent energy is the distance of the melt from at some time, *s(t)*, multiplied by the material latent heat, $H_{f,eff}$, and its density. Equations (10) and (11) both calculate the sensible heat by integrating the temperature difference with respect to distance and multiplying with the appropriate specific heat value, $c_{p,eff}$, and the density. Equation (10) is the energy in the PCM volume between the constant temperature boundary surface and the melt-front that has undergone a full phase change. The first term of Equation (10) is the energy in raising the temperature from the initial temperature to the melting temperature; the second term is the energy in the observed temperature increase above the melting temperature. Similarly, equation (11) calculates the energy in the material beyond the melt-front by integrating the difference in temperature from the initial temperature. It is important to remember that this model assumes an infinite plane, therefore all energies will be reported per square area, [J-cm^{-2}].

$$Q''_{lat}(t) = s(t) * H_{f_{eff}} * \rho_{l_{eff}} \quad (9)$$

$$Q''_{sensible,melted}(t) = (T_m - T_i) * s(t) * c_{p,s_{eff}} * \rho_{s_{eff}} + c_{p,l_{eff}} * \rho_{l_{eff}} * \int_0^{s(t)} (T(x,t) - T_m)dx \quad (10)$$

$$Q''_{sensible,frozen}(t) = c_{p,s_{eff}} * \rho_{s_{eff}} * \int_{s(t)}^{\infty} (T(x,t) - T_i)dx \quad (11)$$

The total energy, $Q_{tot}^{"}$, of the PCM is found by summing equations (9-11). The thermal charging is defined as the total energy calculated at some time and divided by that elapsed time. The thermal charging is representative of the average thermal power pulled into the system for the elapsed time and is shown by Equation (12), [W-cm^{-2}]. The instantaneous power at each time is the slope of this line, [W-s^{-1}-cm^{-2}].

$$P^{"}(t) = \frac{Q_{tot}^{"}(t)}{t} \tag{12}$$

4. RESULTS

The time-temperature plots of the samples are shown by **Figure 2**Figure 2. Note that each sample takes a significantly different length of time to complete due to the different thermal conductivity of the samples, thus each horizontal axis is different. All samples follow the same trend as the model; a fast response to the thermal impulse at the start followed by a slowing of the temperature rise towards the melting point. The end of the melting process is easily discernable as an upward concave inflection point. The start of the melting process is more difficult to identify, however, as the temperature more slowly rises to the melting point in the approach. The analytical solution suggests that each spatial point completes the melting process in infinitesimal time. Since the thermocouples have a nonzero thickness, there should be a finite period at which the thermocouple is reading a near-constant temperature equal to the melting temperature. The temperature glide of the octadecane prevents this constant temperature reading from occurring in the nearest thermocouples. The farthest thermocouple does have a more extended period of near-constant temperature, but this may be due to the lower heat flow being far from the heated surface.

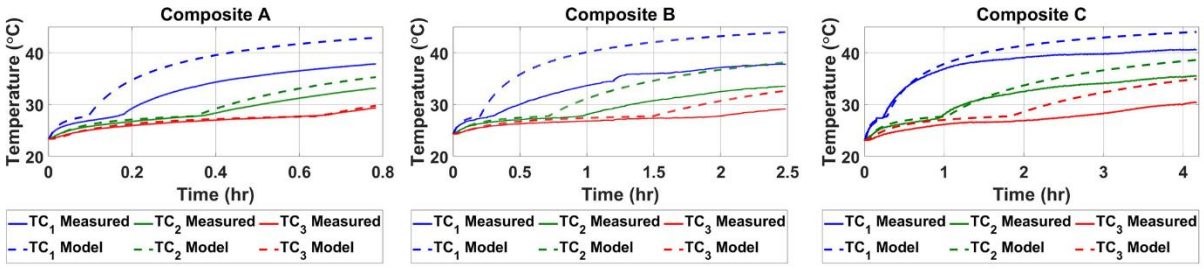

Figure 2: Time-Temperature Measurements of Composite PCMs

For the results in Figure 2, the model predicts higher final temperatures at all thermocouple locations. This difference may be attributed to the deviations from experimental approximations outlined above, particularly unwanted heat loss through the walls of the container and insulation. Future experimental redesign and subsequent testing may be able to address this deviation from model predictions.

The melt-front progression is analyzed by calculating the time each of the thermocouple locations finish the melting process. With the thermocouples' known and fixed distance from the heated surface, the melt-front is fitted to a function with the square root of time to match the analytical solution shown by equation (8). The intercept is set at 0 mm. The form of the fitted melt-front progression is shown by equation (13).

$$s(t)_{fitted} = A_{fitted} * \sqrt{t} + 0 \tag{13}$$

Figure 3 shows the comparison to the melt front progression between the different composites and to each analytical solution. All experimental results have a slower melt-front progression than what is predicted by the model. This is to be expected based on the experimental limitations outlined above. Composite A most closely matches the analytical solution, as can be seen in the melt-front and by Figure 2. This composite had the highest graphite fraction and highest thermal conductivity of the samples tested. Composite C had the lowest graphite fraction and thermal conductivity, and therefore took the longest to complete the melting process at all thermocouple locations. However, the first two thermocouples completed melting faster than the model predictions while the third was much slower. This may suggest some nonuniformity in the sample or that the thermal conductivity is higher than what was used in the model calculations and the unwanted heat loss for the long length of the test affected the results of the farthest thermocouple.

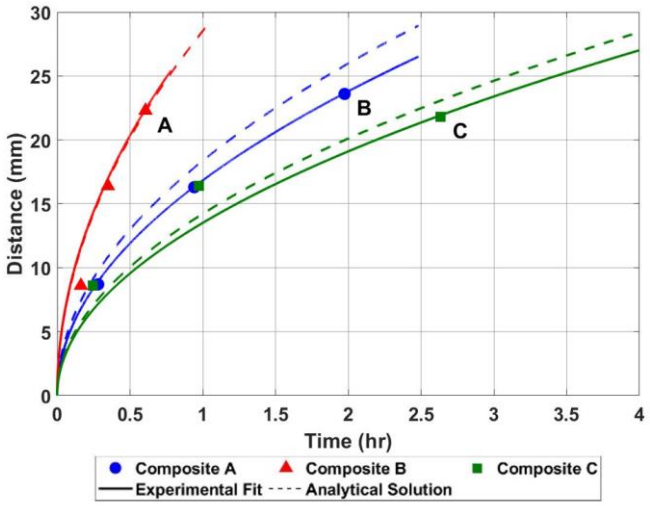

Figure 3: Melt-front progression

Figure 4 shows the thermal charging capacity of the three samples in comparison to the value from the analytical solution. The values are calculated using equations (9-11) at only the three instances when each thermocouple completes the melting process. This may underestimate the thermal energy into the system since the temperature is only known at three discrete points, and there is no interpolation of temperature between the thermocouples or beyond the last. For a real LHTES system, temperature triggers will likely be used in a similar manner to determine the thermal charge of such a system or determining other metrics.

The thermal charging rate of Figure 4 does not have a simple functional form with which to fit the experimental data. As such, the results presented by Figure 4 show only comparison to the analytical solution results as calculated by equation (12). Composites B and C are very similar, differing only slightly in their thermal conductivity. This may explain why the experimental results align well nearest the heated surface but differ at the farthest thermocouple location. Composite A has the highest measured and modeled thermal charging capacity.

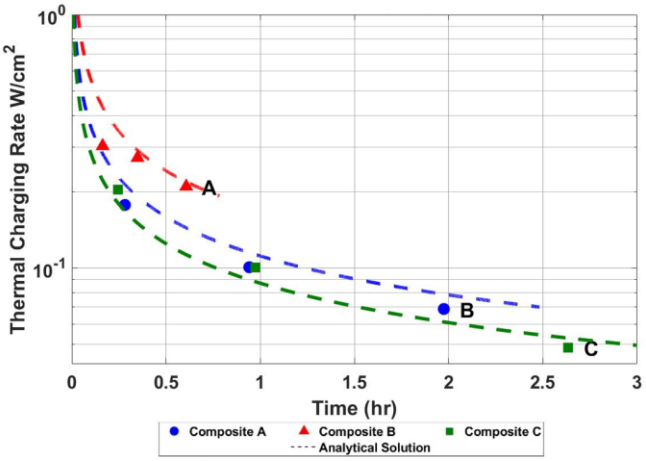

Figure 4: Calculated thermal charging capacity compared to analytical solution

From Table 3, the expected volumetric storage capacity of the samples differ by less than 2%, however, the thermal conductivity of composite A is 3 times that of composite C. In Figure 4, the thermal charging capacity of composite A higher than that of composite C. At the time when the last thermocouple had registered a phase change, Composite A had an average thermal charging capacity of 0.21 W-cm^{-2} and composite C had 0.04 W-cm^{-2}, meaning that

Composite A can store nearly five times the amount of heat than Composite C under the same loading conditions. This demonstrates that the tradeoff between increased thermal conductivity and reduced volumetric storage capacity by the addition of graphite is inconsequential for small graphite amounts.

5. CONCLUSION

For a real application with spatial limitations, there exists a tradeoff between the thermal energy storage capacity [J-m^{-3}] and the thermal charging/discharging capacity [W-m^{-2}] when adding graphite to wax as a thermal conductivity enhancement additive. In this test, three samples were synthesized with n-octadecane and varying amounts of compressed expanded natural graphite (CENG). Across the three composite samples, the thermal conductivity ranged from 0.31 to 0.91 W•$m^{-1}K^{-1}$, compared with 0.2 W•$m^{-1}K^{-1}$for pure octadecane. However, the volumetric storage capacity differed by less than 2% across all samples. This demonstrates that the addition of small CENG amounts can have a profound effect on the thermal conductivity with minimal impacts to the volumetric storage capacity.

The samples were exposed to a constant temperature plate and the melt front proceeding through thermocouples embedded in the sample at various distances away from the constant temperature surface. This was compared to the 1-D semi-infinite analytical phase change solution. The temperature-time plots of the samples follow the melting profile predicted by this analytical solution at the start of the test but deviate as the test progresses. Imperfections in the experimental setup may account for the observed deviation.

The thermal charging rate of the samples was calculated using the expected thermophysical properties and the measured melt-front progression. The thermal charging rate is the average thermal power added to the PCM during the time to reach a fully melted state at a depth of 22 mm under a constant temperature boundary surface. The sample with the highest thermal conductivity had nearly 430% higher average thermal charging rate than the sample with the lowest thermal conductivity. The addition of 5.75% mass fraction CENG decreased the time to melt a depth of 22 mm of PCM by 75% with only a 5% loss in volumetric storage capacity. The thermal conductivity of the PCM composite with 5.75% mass fraction CENG was increased over 450% than that of pure octadecane.

NOMENCLATURE

PCM	Phase Change Material	
LHTES	Latent Heat Thermal Energy Storage	
CENG	Compressed Expanded Natural Graphite	
T	Temperature	(°C)
x	Distance	(m)
t	Time	(sec)
s	Melt-front	(m)
k	Thermal Conductivity	(W-m^{-2}-K^{-1})
ρ	Density	(kg-m^{-3})
H	Latent Heat	(J-kg^{-1})
λ	Numerically-solved parameter	
α	Thermal Diffusivity	(m^2-s^{-1})
Q	Heat	(J)
c	Specific Heat	(J-kg^{-1}-K^{-1})
P	Power	(W)
M	Mass	(kg)
A	Fitted-parameter	(m-$t^{-1/2}$)

Subscripts/Superscripts

l	Liquid
o	Boundary
s	Solid
i	Initial
m	Melting
f	Fusion

lat	Latent	
eff	Effective Composite Properties	
sensible	Sensible heating	
p	Isobaric	
tot	Total	
CENG	CENG	
Octadecane	Octadecane	
γ	Fraction	
fitted	Fitted solution using least squares regression	
"	Per unit area	(m^{-2})

REFERENCES

Abdulateef, A. M., Abdulateef, J., Sopian, K., Mat, S., & Ibrahim, A. (2019). Optimal fin parameters used for enhancing the melting and solidification of phase-change material in a heat exchanger unite. *Case Studies in Thermal Engineering*, 100487. doi:https://doi.org/10.1016/j.csite.2019.100487

Esapour, M., Hamzehnezhad, A., Rabienataj Darzi, A. A., & Jourabian, M. (2018). Melting and solidification of PCM embedded in porous metal foam in horizontal multi-tube heat storage system. *Energy Conversion and Management, 171*, 398-410. doi:https://doi.org/10.1016/j.enconman.2018.05.086

Faden, M., Höhlein, S., Wanner, J., König-Haagen, A., & Brüggemann, D. (2019). Review of Thermophysical Property Data of Octadecane for Phase-Change Studies. *Materials (Basel, Switzerland), 12*(18), 2974. doi:10.3390/ma12182974

Fashandi, M., & Leung, S. N. (2018). Sodium acetate trihydrate-chitin nanowhisker nanocomposites with enhanced phase change performance for thermal energy storage. *Solar Energy Materials and Solar Cells, 178*, 259-265. doi:https://doi.org/10.1016/j.solmat.2018.01.037

Hahn, D. W., & Özişik, M. N. (2012). Heat Conduction Fundamentals. In *Heat Conduction*: Wiley.

Incropera, F. P., & DeWitt, D. P. (2002). *Fundamentals of heat and mass transfer* (5th ed. ed.). New York :: J. Wiley.

Liang, W., Zhu, H., Wang, R., Wang, C., Zhu, Z., Sun, H., & Li, A. (2018). Superhydrophobic Copper Foam Supported Phase Change Composites with High Thermal Conductivity for Energy Storage. *Materials Research*, 0-0.

Mahdi, J. M., Lohrasbi, S., Ganji, D. D., & Nsofor, E. C. (2018). Accelerated melting of PCM in energy storage systems via novel configuration of fins in the triplex-tube heat exchanger. *International Journal of Heat and Mass Transfer, 124*, 663-676. doi:https://doi.org/10.1016/j.ijheatmasstransfer.2018.03.095

Mallow, A., Abdelaziz, O., & Graham, S. (2018). Thermal charging performance of enhanced phase change material composites for thermal battery design. *International Journal of Thermal Sciences, 127*, 19-28. doi:https://doi.org/10.1016/j.ijthermalsci.2017.12.027

Rao, Z., Wen, Y., & Liu, C. (2018). Enhancement of heat transfer of microcapsulated particles using copper particles and copper foam. *Particuology*. doi:https://doi.org/10.1016/j.partic.2017.12.010

Wang, J., Huang, X., Gao, H., Li, A., & Wang, C. (2018). Construction of CNT@Cr-MIL-101-NH2 hybrid composite for shape-stabilized phase change materials with enhanced thermal conductivity. *Chemical Engineering Journal, 350*, 164-172. doi:https://doi.org/10.1016/j.cej.2018.05.190

Yang, X., Bai, Q., Zhang, Q., Hu, W., Jin, L., & Yan, J. (2018). Thermal and economic analysis of charging and discharging characteristics of composite phase change materials for cold storage. *Applied Energy, 225*, 585-599. doi:https://doi.org/10.1016/j.apenergy.2018.05.063

Zeng, J.-L., Chen, Y.-H., Shu, L., Yu, L.-P., Zhu, L., Song, L.-B., . . . Sun, L.-X. (2018). Preparation and thermal properties of exfoliated graphite/erythritol/mannitol eutectic composite as form-stable phase change material for thermal energy storage. *Solar Energy Materials and Solar Cells, 178*, 84-90. doi:https://doi.org/10.1016/j.solmat.2018.01.012

ACKNOWLEDGEMENT

This material is based upon work supported by the U. S. Department of Energy's Building Technologies Office under Contract No. DE-AC05-00OR22725 with UT-Battelle, LLC. The authors would like to acknowledge Mr. Sven Mumme, Technology Manager, U.S. Department of Energy Building Technologies Office.